Journal of Materials Chemistry A

Precision Surface Modification of Solid Oxide Fuel Cells via Layer-by-Layer Surface Sol-Gel Deposition

Journal:	*Journal of Materials Chemistry A*
Manuscript ID	TA-ART-01-2022-000458.R1
Article Type:	Paper
Date Submitted by the Author:	25-Feb-2022
Complete List of Authors:	Kane, Nicholas; Georgia Institute of Technology, School of Materials Science and Engineering Zhou, Yucun; Georgia Institute of Technology, School of Materials Science and Engineering Zhang, Weilin; Georgia Institute of Technology, School of Materials Science and Engineering Ding, Yong; Georgia Institute of Technology, School of Materials Science and Engineering Luo, Zheyu; Georgia Institute of Technology, Materials Science and Engineering Hu, Xueyu; Georgia Institute of Technology, School of Materials Science and Engineering Liu, Meilin; Georgia Institute of Technology, School of Materials Science and Engineering

Precision Surface Modification of Solid Oxide Fuel Cells via Layer-by-Layer Surface Sol-Gel Deposition

Nicholas Kane,[a] Yucun Zhou,[a] Weilin Zhang,[a] Yong Ding,[a] Zheyu Luo,[a] Xueyu Hu,[a] and Meilin Liu*[a]

[a] School of Materials Science and Engineering, Georgia Institute of Technology, 771 Ferst Dr. NW, Atlanta, GA, 30332-0245, USA. E-mail: meilin.liu@mse.gatech.edu

† Electronic supplementary information (ESI) available.

Keywords: surface modification, surface sol-gel, solid oxide fuel cell, catalyst

Abstract

While solid oxide fuel cells (SOFCs) are a promising technology for a clean and sustainable future, their commercialization is hindered by limited durability and performance. Here, we report our findings in the application of a layer-by-layer surface sol-gel (SSG) coating of catalysts to dramatically enhance the electro-catalytic activity and durability of SOFC cathodes. The SSG process is capable of penetrating and preserving complex backbone microstructures of porous electrodes, creating highly conformal coatings of controlled morphology, while tailoring the composition of the surface to improve catalytic properties and durability. For example, the application of an SSG coating of PrO_x to a $La_{0.6}Sr_{0.4}Co_{0.2}Fe_{0.8}O_{3-\delta}$ (LSCF) cathode has reduced the polarization resistance from 1.136 to 0.117 Ω cm^2 at 600 °C and the degradation rate from 1.13×10^{-3} to 2.67×10^{-4} Ω cm^2 h^{-1} at 650 °C. In addition, a continuous improvement in electrode performance is demonstrated as the thickness of the coating is increased, corresponding to the linear addition of catalyst. This first application of the SSG technique to SOFC systems opens the door for the controlled surface modification of porous components in electrochemical systems.

Introduction

Solid oxide fuel cells (SOFCs) are one of the most efficient and promising options for large scale energy conversion because they can generate electricity directly from fuels with high efficiency. However, breakthroughs in materials innovation are required for SOFCs to be implemented on a large scale, as several challenges remain to be fully resolved. Performance is limited by slow rates for oxygen reduction reactions (ORR) on the cathode [1]. Additionally, widespread use is limited by inadequate durability, causing increased system costs. Due to the high operating temperature of the cells, multiple degradation mechanisms are present and degradation of the electrode materials is accelerated [2, 3]. Surface modification of SOFC electrodes with a catalyst is a very effective approach to increase tolerance to contaminant poisoning and improve catalytic properties, thus increasing electrode performance and durability [4-9]. Solution infiltration has been widely utilized to apply catalytic coatings [10-14]; however, this technique suffers from significant drawbacks. The infiltration must be uniform across the entirety of the backbone but drying of the solvent can induce inhomogeneous deposition and agglomeration of metal salt crystals [1]. Solution concentrations, additives such as polymeric surfactants, viscosity, and solvent choice all affect the distribution and morphology of the resulting deposition [15]. The porosity, morphology, and tortuosity of the backbone all effect the infiltration process as well, which can lead to varied results and unstable process control. In addition, multiple infiltration-calcination cycles is normally needed to ensure a sufficient catalyst loading, which is time consuming and not cost-efficient. These drawbacks create the need for a more controllable surface modification process, such as surface sol-gel.

The surface sol-gel process, first introduced by Ichinose et al.[16, 17], is analogous to atomic layer deposition in the liquid phase. The process, which is schematically depicted in **Figure 1(a)**,

can be described in two main steps; the first is chemisorption of a metal alkoxide to the substrate surface via a reaction with surface hydroxyls. The following step is aqueous hydrolysis of the chemisorbed layer to form an oxide and reform surface hydroxyl groups. Each reaction is self-limiting, stopping once all the surface hydroxyls or organic ligands have reacted. Thus, by alternating solutions, the surface modification can be built up layer by layer. This process can generate conformal coatings throughout complex porous structures, as chemisorption of the alkoxide is limited by available surface hydroxyls [18-21]. Precise thickness control can be achieved by adjusting the number of the hydrolysis-condensation cycles. Another advantage of the surface sol-gel process is low cost and excellent scalability, as the precursors and equipment are significantly cheaper than atomic layer deposition. In addition, multiple calcinations are not necessary since the coating can be calcined 'in-situ' at low temperatures during the initial ramp. A wide variety of metal alkoxides have already been developed for more traditional sol-gel processes, allowing the surface sol-gel process to quickly expand to new material systems. In this paper, the surface sol-gel process is applied to solid oxide fuel cells for the first time, using PrO_x on $La_{0.6}Sr_{0.4}Co_{0.2}Fe_{0.8}O_{3-\delta}$ (LSCF) as a model to demonstrate the feasibility and capability of this process. The morphology and electrochemical performance are carefully controlled by adjusting the number of coating cycles. The catalyst loading is shown to correlate closely to the number of coating cycles, which have a direct impact on the activation energy, polarization resistance, and degradation rate of cathodes. The process presented here is not limited to PrO_x on LSCF, but can be expanded to a variety of different catalysts, electrode materials, and electrochemical systems.

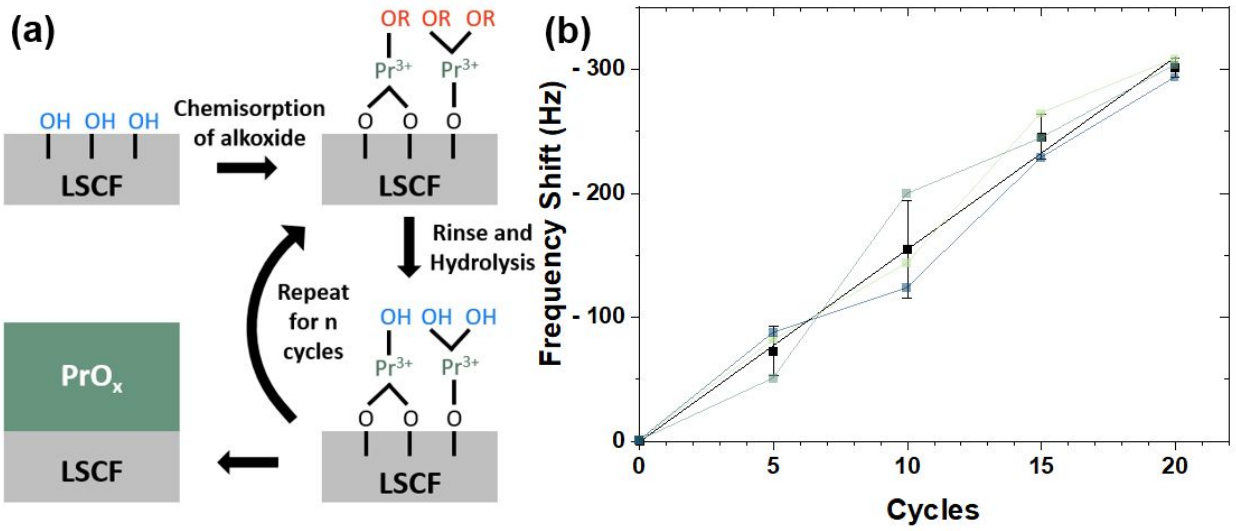

Figure 1. (a) Schematic diagram of the surface sol-gel process showing the chemisorption and hydrolysis of praseodymium(III) isopropoxide to form PrO_x. (b) Frequency shift versus deposition cycle count for PrO_x measured via quartz crystal microbalance.

Results and Discussion

The deposition of PrO_x on a quartz crystal microbalance (QCM) was tracked over 20 cycles for multiple sensors. Figure 1(b) shows the QCM frequency shift as a function of cycle count. The data show that the frequency decreases linearly with the cycle count, indicating that each cycle deposits an equal and controlled amount of PrO_x on the surface. Thus, linear growth is achieved with praseodymium(III) isopropoxide ($Pr(O^iPr)_3$), verifying the stepwise adsorption and hydrolysis of the alkoxide. Additionally, the QCM data was used to estimate the mass change per area via the Sauerbrey equation ($\Delta m = -C\Delta f/n$, where m is the mass normalized by area, C is constant dependent on the crystal used, n is the overtone number, and f is the frequency. For the crystal used in this work, $C = 17.7$ ng cm^{-2} Hz^{-1}, and the third harmonic was used, $n = 3$). The slope of the linear regression line in Figure 1b is 15.5 Hz/cycle, thus the mass of catalyst added per cycle is calculated to be 91.4 ng cm^{-2}. The surface area of an identical electrode was measured in a

previous paper to be 0.8 $m^2 g^{-1}$ [13]. With an average ¼" electrode mass of 2.35 mg, the mass of the catalyst added for a two sided symmetrical cell is estimated to be 3.44 μg per cycle.

Figure 2 shows the STEM and energy-dispersive X-ray (EDX) spectroscopic analysis of the surface modification of LSCF with 15 cycles of $Pr(O^iPr)_3$. The catalyst-coated LSCF electrodes are denoted with the cycle count, i.e., 15-PrO_x-LSCF. EDX maps were taken on the edge of the LSCF particle to observe the thickness and composition of the catalyst particles. It is important to note that the LSCF particle was not cross sectioned. Thus, the 'Bulk' section in the STEM image and the 'Bulk' EDX spectrum also contains surface catalyst particles. The overlap between the Pr $L\alpha_1$ $L\alpha_2$ peaks (at 5.033 and 5.013 keV) and the La $L\beta_1$ peak (at 5.042 keV), as well as the Pr $L\beta_1$ peak (at 5.488 keV) and the La $L\beta_2$ peak (at 5.383 keV), makes it difficult to differentiate La from Pr when both La and Pr are present [22]. However, the La $L\alpha_1$ and $L\alpha_2$ peaks (at 4.650 and 4.634 keV) do not coincide with any peaks corresponding to Pr, Co, Fe, or O. Thus, the absence of a peak around 4.6 keV allows the peaks at 5 and 5.4 keV to be attributed to Pr. EDX spectra were taken on the bulk and the surface of the backbone particle. The bulk shows the presence of La, Sr, Co, and Fe from the LSCF backbone, while it is difficult to resolve the Pr peaks. Conversely, the surface particles only show the presence of the Pr and O, excluding Cu from the TEM grid. Thus, it is concluded that there is no diffusion of the LSCF backbone into the PrO_x particles, which remain a distinct phase on the surface. **Figure S2** shows the X-ray diffraction (XRD) analysis of the $Pr(O^iPr)_3$ precursor reacted with water after annealing at different temperatures and reacted in the presence of LSCF. The data show that the resulting phase is Pr_6O_{11}. Additionally, the phase formation is unaffected by LSCF and there is no significant reaction observed between LSCF and Pr_6O_{11} at 650 °C after 10 hours. The XRD shows that two distinct phases remain, which is consistent with the STEM EDX results, showing the surface particles consist only of PrO_x. **Figure**

S3 shows a direct comparison of the LSCF+Pr(O^iPr)$_3$ sample with the commercial LSCF powder. No significant shift in peak positions is observed. Since there is no exposure to temperatures exceeding 650 °C after modification of the LSCF, reaction/diffusion between the LSCF and Pr_6O_{11} is severely limited. Thus it is concluded that the PrO_x remains a distinct phase on the surface, which has been reported previously.[11, 23]

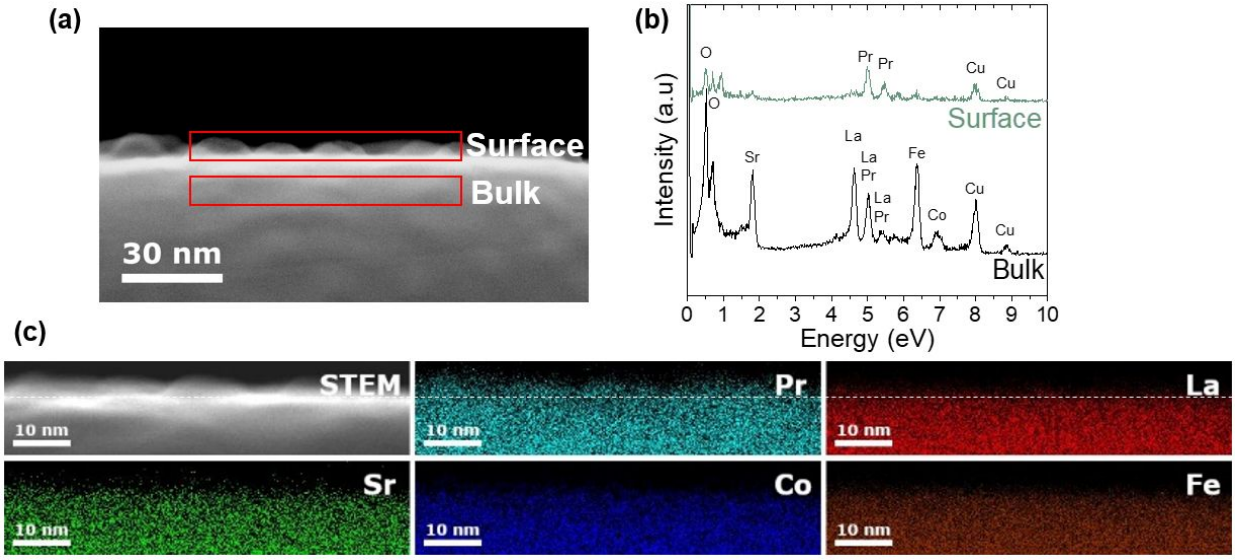

Figure 2. STEM EDX characterization of 15-PrO_x-LSCF. (a) STEM image of the edge of a 15-PrO_x-LSCF particle, highlighting the scan location of the bulk and surface spectra. (b) EDX spectra of the surface particles and bulk 15-PrO_x-LSCF. (c) EDX mapping of the same location on 15-PrO_x-LSCF showing the presence of Pr containing particles on the surface of the LSCF.

The high-resolution STEM images of 15-PrO_x-LSCF and 45-PrO_x-LSCF after firing at 650 °C for 2 hours are shown in **Figure 3**. The images show the presence of nanoparticles on the surface of the LSCF backbone particle. The 15-PrO_x-LSCF contains small, isolated, finely dispersed nanoparticles on the order of 5 to 20 nm in diameter, with a thickness around 5 nm, as shown in Figure 2(a). In contrast, the 45-PrO_x-LSCF shows much higher surface coverage, with many particles connecting together to form a more continuous phase. The estimated surface coverage calculated from microscopic analysis was 23% and 67%, for the 15-PrO_x-LSCF and 45-PrO_x-LSCF, respectively. For the higher cycle counts, a few agglomerates on the order of 50 nm are

seen. STEM EDX, shown in **Figure S4**, verifies these agglomerates are also PrO_x through a similar analysis. Figure 3(d) shows the surface modification is uniform across the entire particle. The morphology of the surface modification can be seen from the clear contrast between smooth bare LSCF areas, which were exposed during sample preparation for STEM, and the rest of the particle. **Figure S5** and **Figure S6** highlight the uniformity of the surface modification over a large area of the cross section of the electrode. These SEM images show that the SSG surface modificaiton evenly coats the entirety of the electrode, leaving no unmodified areas which are commonly seen in porous electrodes modified using a traditional solution infiltration process [24-29]. Additionally, the PrO_x particle size and spacing are extremely homogenous across the electrode and there are no large agglomerations of modification particles. **Figure S7** shows the morphology of 15-PrO_x-LSCF and 45-PrO_x-LSCF before and after the 200 hour stability test at 650°C, which shows that the surface modified particles coarsened over the duration of the test.

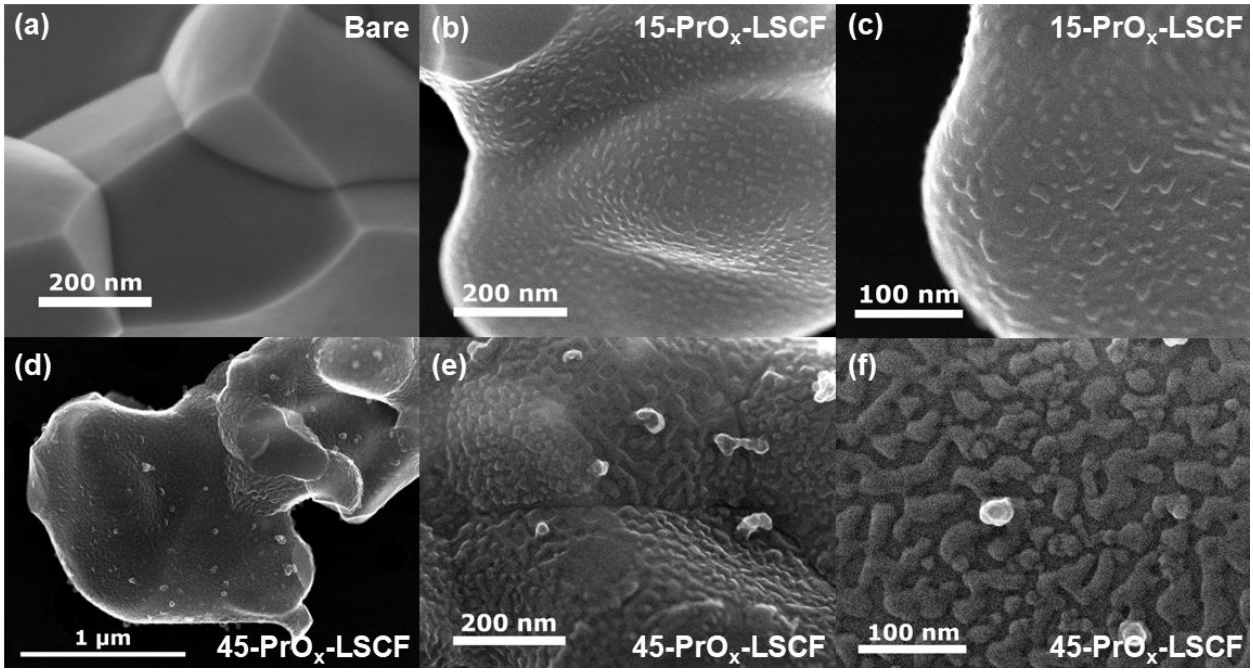

Figure 3. High resolution characterization of PrO_x modified LSCF. SEM images of (a) unmodified LSCF at 150k magnification. STEM images of (b-c) 15-PrO_x-LSCF at 150k and 300k magnification and (d-f) 45-PrO_x-LSCF at 50k, 150k and 300k magnification after firing at 650 °C for 2 hours.

The electrochemical impedance analysis of the electrolyte supported symmetrical cells is shown in **Figure 4**. Figure 4(a) shows the activation energy plot for bare LSCF, 75-PrO_x-LSCF, and other recently reported publications, including $Ba_{1-x}Co_{0.7}Fe_{0.2}Nb_{0.1}O_{3-\delta}$-$BaCO_3$ infiltrated LSCF[13], $PrNi_{0.5}Mn_{0.5}O_3$-PrO_x infiltrated LSCF [30], $PrBa_{0.2}Ca_{0.2}Co_2O_{5-\delta}$ (PBCC) [31], PrO_x infiltrated LSCF [11], $PrO_{2-\delta}$ infiltrated a-site-deficient LSCF [23], and $BaCoO_{3-\delta}$ infiltrated LSCF [12]. The data show that the SSG modification has a lower polarization resistance than similar PrO_x surface modifications fabricated via solution infiltration, and is even lower than that of recently reported state-of-the-art PBCC. The effect of temperature and cycle count on the R_p is shown in **Figure S8**. The increase in deposition cycles is shown to decrease the R_p at all temperatures, with more benefit at lower temperatures, attributed to the decreased activation energy of the coated cells as compared to the bare cells. For example, at 600 °C, the R_p decreased from 1.136 Ω cm^2 to 0.117 Ω cm^2, and at 500 °C, the R_p decreased from 27.41 Ω cm^2 to 0.991 Ω cm^2, making the R_p of 75-PrO_x-LSCF just 1/10 and 1/30 of the bare LSCF. The activation energy was also shown to be a function of the cycle count. Activation energy decreased as the cycle count increased, as more catalyst was deposited on the surface of the electrode, decreasing from 1.73 eV for bare LSCF to 1.33, 1.41, 1.32, 1.39, 1.20, 1.08, and 1.07 eV for the 5, 10, 15, 30, 45, 60, and 75-PrO_x-LSCF, respectively. The data also shows the optimization of the coating cycle count. At lower temperatures, R_p continually decreases up to 60 cycles, while at higher temperatures, only 45 cycles are required to achieve the maximum catalytic effect.

The polarization resistance was tracked over 200 hours of operation at 650 °C, as shown in Figure 4(b). In addition to decreasing initial R_p, the PrO_x surface modification also decreased the degradation rate of the LSCF cathode. The amount of catalyst, carefully controlled via the number of cycles, is shown to affect both the initial R_p, as well as the stability of the R_p. The

degradation rate was decreased drastically, decreasing from 1.13×10^{-3} Ω cm^2 h^{-1} for the bare LSCF, to 8.57×10^{-4}, 7.74×10^{-4}, 6.15×10^{-4}, 2.49×10^{-4}, 2.81×10^{-4}, and 2.67×10^{-4} Ω cm^2 h^{-1} for the LSCF modified with 5, 10, 15, 30, 60, and 75 cycles, respectively. Notably, the 30-PrO_x-LSCF, 60-PrO_x-LSCF, and 75-PrO_x-LSCF decreased the degradation rate at 650 °C by a factor of 5 compared to the unmodified cell.

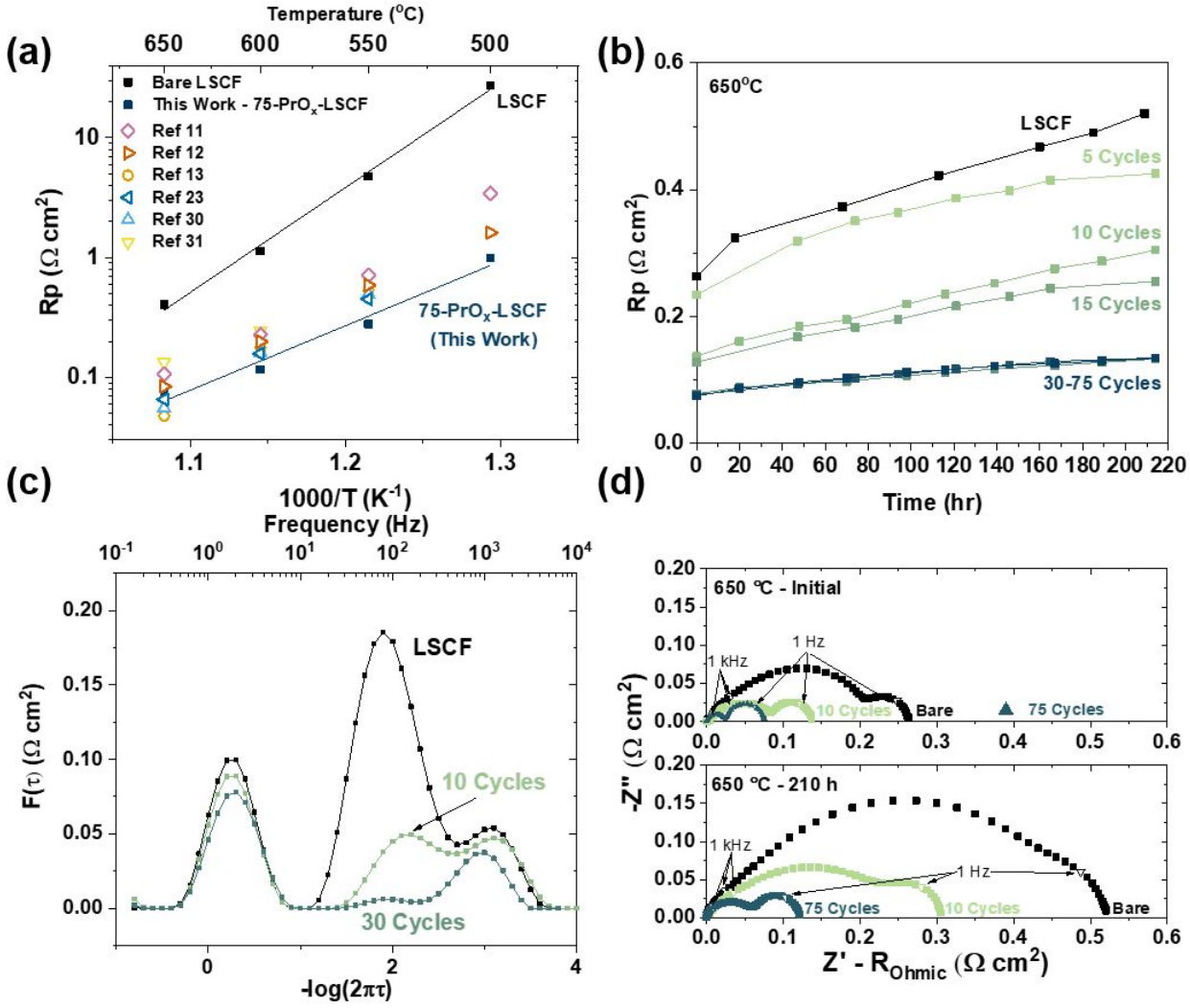

Figure 4. Electrochemical impedance spectroscopy analysis. (a) Initial (t = 0 hr) activation energy plots between 500 and 650 °C of bare LSCF, 75-PrO_x-LSCF and recent publications, including $Ba_{1-x}Co_{0.7}Fe_{0.2}Nb_{0.1}O_{3-\delta}$-$BaCO_3$ infiltrated LSCF[13], $PrNi_{0.5}Mn_{0.5}O_3$-PrO_x infiltrated LSCF [30], $PrBa_{0.2}Ca_{0.2}Co_2O_{5-\delta}$ [31], PrO_x infiltrated LSCF [11], $PrO_{2-\delta}$ infiltrated a-site-deficient LSCF [23], and $BaCoO_{3-\delta}$ infiltrated LSCF [12]. (b) Polarization resistance as a function of time at 650 °C for bare LSCF and PrO_x modified LSCF. (c) Distribution of relation times for bare LSCF, 10-PrO_x-LSCF, and 30-PrO_x-LSCF at 650 °C. (d) Nyquist plots of bare LSCF, 10-PrO_x-LSCF, and 75-PrO_x-LSCF before (top) and after (bottom) 210 hours at 650 °C.

Distribution of relaxation time (DRT) analysis, shown in Figure 4(c), was performed in order to deconvolute the impedance spectra. Three main processes were identified, including a low frequency process around 1 Hz, an intermediate frequency process around 100 Hz, and a high frequency process around 1 kHz. Figure 4(c) shows the intermediate frequency process, which is typically attributed to surface oxygen exchange processes [6], was greatly affected by the PrO_x surface modification, reducing the resistance of this process (R_{IF}) from the most resistive to the least. Little effect is seen on the low and high frequency processes. This indicates that the rate limiting step is changing from the intermediate frequency processes to the low and high frequency processes. Electrical conductivity relaxation (ECR) measurements, shown in **Figure S9**, verify the increase in surface exchange kinetics. **Figure S10** shows the surface modification particles are uniformly distributed across the dense LSCF bar. The 30-PrO_x-LSCF bar demonstrated superior exchange kinetics, reducing the equilibration time from 13000 s to 6500 s (**Figure S9**), as compared to the bare LSCF, and the calculated surface exchange coefficient, k, increased from 2.11×10^{-5} for the bare LSCF to 5.91×10^{-5} cm s^{-1} for the 30-PrO_x-LSCF. Additionally, the decrease in impedance is more pronounced at lower temperatures, which can be attributed to the fact that the impedance of the intermediate processes dominates at lower temperatures (see **Figure S11**). Thus, the surface modification has a greater benefit on the overall cell impedance at lower temperatures. Conversely, at higher temperatures, the resistance of the intermediate process is greatly reduced by thermal activation, so the ability of the surface modification to reduce the impedance is diminished. The catalytic enhancement of the surface sol-gel modification is clearly seen in Figure 4(d) as a decrease in the total polarization resistance, decreasing from 0.263 Ωcm^2 for the bare LSCF to 0.075 Ω cm^2 for the 75-PrO_x-LSCF at 650 °C. After 210 hours at 650 °C, the R_p increased to 0.520 and 0.134 Ω cm^2 for the bare LSCF and 75-PrO_x-LSCF, respectively.

The DRT analysis shown in **Figure 5(a)** compares the DRT of bare and various cycle counts before and after the 210 h stability test, which shows that the increase in polarization resistance is associated with the intermediate frequency process. This is likely due to surface strontium segregation, decreasing the surface reaction kinetics [14]. Additionally, the PrO_x particles coarsened over the duration of the test, as shown in **Figure S7**, which could contribute to the increase in polarization resistance over time. Figure 5(a) shows that the cells with higher catalyst loading (e.g., 75-PrO_x-LSCF) suppressed the increase of R_{IF} as compared with lower catalyst loadings (e.g., 10-PrO_x-LSCF). This is consistent with the stability data in Figure 4(b), which shows higher stability for the higher catalyst loaded cells. Thus, it is concluded that the PrO_x surface modification creates a more stable surface for the ORR. Figure 5(a) also shows that additional cycles above 30 cycles are ineffective at 650 °C because the impedance of the intermediate frequency process is already completely reduced to zero, thus increasing the catalyst loading has no further effect on the polarization resistance.

The integral of the DRT curves represents the polarization resistance, allowing an impedance to be calculated for each process. Additionally, the polarization resistance changes with the partial pressure of oxygen according to $R_p = k(p_{O2})^{-n}$ [6]. The dependence on the partial pressure of oxygen, represented by the n value, can then be used to identify the processes occurring. The effect of partial pressure of oxygen on the polarization resistance of each process, R_{LF}, R_{IF}, and R_{HF}, is shown in Figure 5(b-c). Gaussian fitting was applied to the DRT curves to calculate the integral area of each peak and thus the corresponding polarization resistance. The low frequency process was greatly dependent on pO_2, with n = ~1.45. Thus, this low frequency process can be attributed to gas diffusion within the electrode, which is consistent with other studies [32-34]. The surface modification showed negligible change on the resistance of this process, which helps

confirm the backbone structure and porosity of the cathode was preserved through the surface modification. The intermediate frequency process shows a dependence on pO_2 with n = 0.10 for the bare LSCF and n = 0.52 for the 30-PrO_x-LSCF, indicating the rate limiting step of the ORR may be changing with the addition of the surface modification. An n of 0.25 is typically associated with charge transfer processes with electrons and O^{2-}, while an n of 0.5 corresponds to the adsorption ($O_2 \rightarrow O_{2,ads}$) and dissociation ($O_{2,ads} \rightarrow 2O_{ads}$) process of oxygen [6, 35]. Jørgenson et al. concluded that the intermediate frequency process is the combination of the various steps comprising the overall ORR [36]. The addition of the catalyst modification greatly reduces the impedance of the rate limiting step. It can also be seen that the surface modification has relatively little effect on the high frequency process, which is attributed to the charge transfer process as the n of 0.29 is very close to 0.25. As with R_{LF}, R_{HF} shows little change with the addition of the catalyst, thus it is concluded the PrO_x surface modification has little effect on this process.

The impedance results clearly demonstrate the powerful capability of the layer-by-layer growth. The incremental catalyst addition directly correlates with the electrochemical impedance response, which shows corresponding decreases in the activation energy and degradation. SEM images also confirm the increase in catalyst loading and surface coverage for higher cycle counts. These results highlight a key benefit of SSG, allowing the amount of catalyst to be carefully controlled and adjusted. The stepwise fashion in which catalyst is applied to the cell allows for the identification of the maximum amount of expensive catalyst that should be used, potentially reducing cost. The careful evaluation of catalyst loading can ultimately lead to the rational design of surface modifications with optimized catalyst loadings.

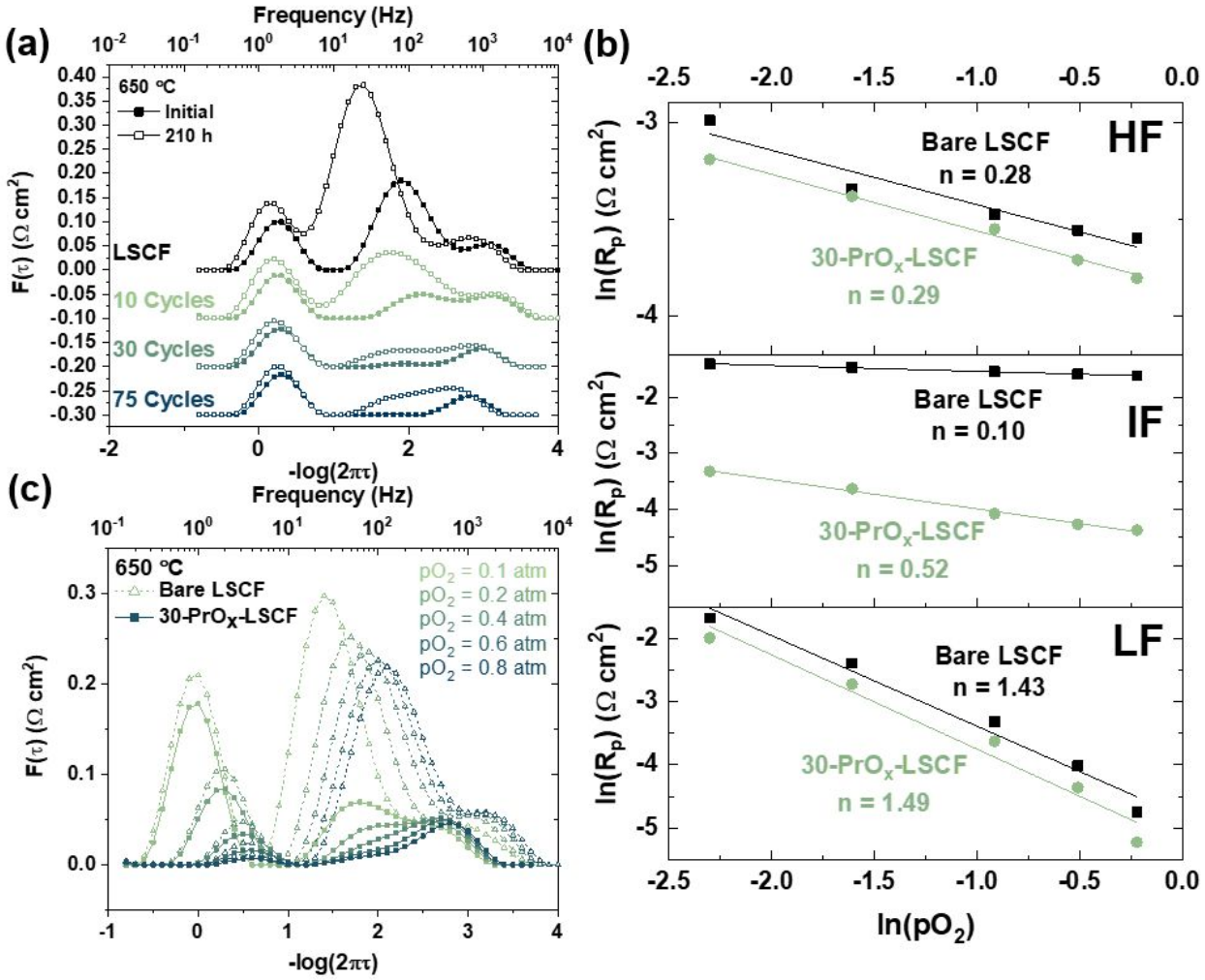

Figure 5. Distribution of relaxation time analysis. (a) DRT plots of bare and coated LSCF before (solid markers) and after (open markers) 210 hours at 650 °C. (b) Polarization resistance of the high, intermediate, and low frequency processes as a function of partial pressure of O_2 for bare LSCF (black) and 30-PrO_x-LSCF (green). (c) DRT plots of bare LSCF (open markers) and 30-PrO_x-LSCF (solid markers) at different partial pressures of O_2 from 0.1 atm to 0.8 atm at 650 °C.

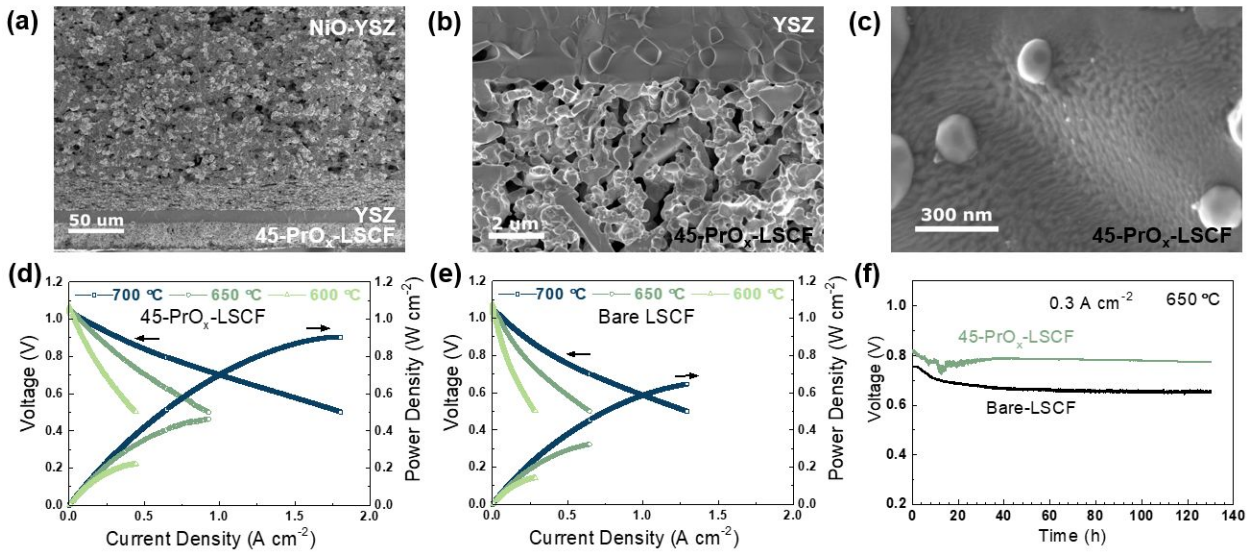

Figure 6. Surface sol-gel modification of LSCF|SDC|YSZ|Ni-YSZ single cells with 45 cycles of PrO_x. SEM images of (a) the anode supporting layer, anode functional layer, electrolyte, and cathode, (b) the electrolyte cathode interface, and (c) the cathode surface modification. Comparison of the peak power density of (d) 45-PrO_x-LSCF and (e) bare LSCF single cells. Stability of 45-PrO_x-LSCF and bare LSCF single cells at 0.3 A cm^{-2} at 650 °C.

YSZ-based single cells were fabricated and tested to further verify the enhanced ORR activity and stability of the PrO_x catalyst-coated LSCF cathode. For the single cell tests, 45 cycles were chosen as the optimized coating, as symmetrical cell data shows no further improvement with additional cycles at 650 °C. Keeping the cycle count low decreases the overall processing time and costs by minimizing the amount of catalyst precursor and solvent used. SEM images of the YSZ based single cell are shown in **Figure 6(a-c)**, displaying the anode supporting layer (top of the image), anode functional layer, electrolyte, and cathode (bottom of the image). The low-resolution image of the cathode and electrolyte verify the porous backbone structure was preserved (see Figure 6(b)), while the high-resolution image of the cathode surface shows the PrO_x surface modification is uniform across the backbone (see Figure 6(c)). Due to the lower resolution of SEM compared to STEM, it is hard to distinguish the individual particles in Figure 6(c) that are displayed in the STEM image in Figure 3(e); however, these surfaces are similar since they were prepared under identical processing conditions. The performance of an unmodified and 45-PrO_x-LSCF single cell is compared in Figure 6(d-e). The 45-PrO_x-LSCF demonstrated an increased peak

power density of 0.46 W cm^{-2} at 650 °C, compared to 0.32 W cm^{-2} for the bare LSCF. The peak power density is compared to other state-of-the-art LSCF surface modifications in **Table 1**. Notably, the 45-PrO_x-LSCF outperforms LSCF infiltrated with $BaCoO_{3-\delta}$ [12], $PrNi_{0.5}Mn_{0.5}O_3$-PrO_x [7], $Ba_{1-x}Co_{0.7}Fe_{0.2}Nb_{0.1}O_{3-\delta}$-$BaCoO_{3-x}$ [13], $Pr_{0.75}Sr_{0.2}MnO_{3-\delta}$ [37], $PrSrCoMnO_{6-\delta}$ [37], and $La_{0.85}Sr_{0.15}MnO_3$ [38], as well as cells modified with atomic layer deposition, such as Al_2O_3 modified $La_{0.6}Sr_{0.4}CoO_3$ [39] and CoO_x modified $La_{0.8}Sr_{0.2}MnO_3$ [40]. The stability of the single cells is compared in Figure 6(f), which shows that the performance of the 45-PrO_x-LSCF is higher than that of the bare LSCF for the duration of the test. The improvement in performance is attributed to the decrease in the polarization resistance from the catalyst modification, as shown in **Figure S12**. The single cell data verify the SSG catalyst modification can effectively be applied to single cell architectures, increasing both the catalytic activity and stability of the cell.

Table 1. Comparison of the performances of YSZ-based SOFCs with catalyst modified cathodes.

Cathode	Catalyst	Catalyst fabrication method	P_{max} (W cm^{-2})	Reference
LSCF	PrO_x	Solution infiltration	~0.43 (650 ºC)	[11]
LSCF	$BaCoO_{3-x}$	Solution infiltration	0.51 (700 ºC)	[12]
LSCF	$PrNi_{0.5}Mn_{0.5}O_3$-PrO_x	Solution infiltration	0.71 (750 ºC)	[7]
LSCF	$Ba_{1-x}Co_{0.7}Fe_{0.2}Nb_{0.1}O_{3-\delta}$ - $BaCoO_{3-x}$	Solution infiltration	0.86 (700 ºC) 0.46 (650 ºC)	[13]
LSCF	$Pr_{0.75}Sr_{0.2}MnO_{3-\delta}$ $PrSrCoMnO_{6-\delta}$	Solution infiltration	~0.88 (750 ºC) ~0.9 (750 ºC)	[37]
LSCF	$La_{0.85}Sr_{0.15}MnO_3$	Solution infiltration	~0.65 (700 ºC)	[38]
$La_{0.6}Sr_{0.4}CoO_3$	Al_2O_3	Atomic layer deposition	0.87 (700 ºC)	[39]
LSCF	$La_{0.6}Sr_{0.4}CoO_3$	Atomic layer deposition	0.39 (600 ºC)	[41]
$La_{0.8}Sr_{0.2}MnO_3$	CoO_x	Atomic layer deposition	~0.87 (750 ºC)	[40]
LSCF	Pt CoO_x	Atomic layer deposition	~1.3 (750 ºC) ~1.15 (750 ºC)	[42]
LSCF	PrO_x	Surface sol-gel	0.90 (700 ºC) 0.46 (650 ºC) 0.22 (600 ºC)	**This work**

This work demonstrates the powerful capability of surface sol-gel to incrementally modify porous microstructures, which is extremely beneficial within electrochemistry. The technique has great potential for the expansion to new coating materials and porous systems, such as solid oxide electrolysis cells, batteries, and other porous-electrode electrochemical devices.

Conclusion

The layer-by-layer SSG process has been successfully applied to SOFCs to enhance the performance and durability of SOFC cathodes. The PrO_x coatings on LSCF electrodes are shown to be extremely uniform across the electrode particles and electrode as a whole. The catalyst coating increased the catalytic activity and stability of the electrode, decreasing the polarization resistance and the degradation rate at 650 °C by a factor of 5 from 1.13×10^{-3} Ω cm^2 h^{-1} to 2.67×10^{-4} Ω cm^2 h^{-1}. In addition, the layer-by-layer addition of catalyst was clearly demonstrated via QCM and SEM analysis, showing a linear increase in catalyst loading with coating cycles. The electrochemical impedance analysis also demonstrates that the incremental catalyst loading results in stepwise decreases in the activation energy, polarization resistance, and degradation rate. Finally, the optimized coating process was applied to YSZ-based single cells, which demonstrate an improved peak power density of 0.46 W cm^{-2} at 650 °C, compared to 0.32 W cm^{-2} for the cell with unmodified LSCF. This work demonstrates the application of surface sol-gel to porous SOFC electrodes and opens the door for the expansion to new catalyst materials, such as $BaCoO_3$, as well as other electrochemical systems, such as lithium-ion and lithium-air batteries.

Experimental Methods

Deposition Validation with Quartz Crystal Microbalance

The SSG process was first verified using a quartz crystal microbalance to verify the stepwise growth of the film. Deposition was carried out with a custom-built reactor, shown in **Figure S13**, capable of dispensing and draining precursor solutions into a sample chamber. A vacuum pump was used to drain precursor from the reaction chamber, but the top of the chamber was open to air, and thus, the chamber remained at atmospheric pressure. The sample chamber was held at 100 °C. For deposition, the sample was soaked in 5 mM praseodymium(III) isopropoxide ($Pr(O^iPr)_3$) in anhydrous 2-methoxyethanol (2-ME) for 10 minutes to allow for chemisorption of the alkoxide. The sample was then rinsed in anhydrous 2-ME three times, holding the sample in fresh solvent for 30 seconds three consecutive times. The sample was then submerged in 1 vol% DI water in 2-ME for 2 minutes before three more solvent rinses. The entire process (alkoxide, rinse, DI water, rinse) was repeated for a specified number of cycles. The frequency of the gold coated quartz microbalance crystal (Biolin, QSense Analyzer) was measured before and after deposition.

Surface Modification of Cells

SSG coatings of catalysts were applied to $Sm_{0.2}Ce_{0.8}O_{2-\delta}$ (SDC) electrolyte-supported LSCF symmetrical cells (with a configuration of LSCF|SDC|LSCF) and anode-supported single cells (with a configuration of LSCF|SDC|YSZ|Ni-YSZ) [12, 13]. Briefly, electrolyte supported LSCF symmetrical cells were prepared by bonding LSCF tapes onto SDC pellets. The 10 mm SDC pellets were prepared by dry pressing SDC power (Fuel Cell Materials, US) containing 2 wt% polyvinyl butyral and sintering at 1450 °C for 5 hours. LSCF tapes were prepared by tape casting a slurry containing LSCF powder (Fuel Cell Materials, US), graphite, plasticizer, and binder. The ¼" diameter LSCF tapes were bonded to the SDC pellet using an SDC slurry containing SDC powder, V-006 (Heraeus), and acetone, followed by firing at 1080 °C for 2 hours. To fabricate the single cells, NiO-YSZ|YSZ half cells were fabricated by co-tape casting the YSZ electrolyte and

NiO-YSZ supporting and functional layers. The half cells were co-sintered in air at 1400 °C for 4 hours. An SDC barrier layer was fabricated via dip-coating which was subsequently fired at 1250 ºC for 2 hours. The LSCF cathode was brush-painted onto the anode-supported cell and fired at 1080 °C for 2 hours. For modification of a single cell cathode, the anode was masked prior to deposition by coating it with 10 wt% polyvinyl alcohol in DI water which was subsequently dried at 70 °C. The LSCF electrodes were coated with varying numbers of the hydrolysis-condensation cycles from 0 to 75. After coating, the PVA mask on the single cells was removed by soaking in DI water. The PrO_x coating was in-situ calcined at the cell testing temperature during the initial furnace ramp. The active electrode area of the symmetrical and single cells was 0.28 cm^2.

Silver mesh was used as the current collectors for electrochemical measurements. Impedance spectra were acquired over a frequency range of 0.1 Hz to 100 kHz with an AC amplitude of 30 mV using a Princeton Applied Research Parstat MC. Symmetrical cells were measured in ambient air at 500 °C to 650 °C. The partial pressure of O_2 inside a quartz tube housing symmetrical cells was controlled by adjusting the relative flow rates of O_2 and N_2 with a total flow rate of 100 sccm. For single cell measurements, cells were mounted and sealed on an alumina support tube. H_2 with 3 vol% H_2O was used as the fuel, and ambient air was used as the oxidant. The I-V curves of cells were acquired using an Arbin multi-channel electrochemical testing system.

Characterization of the Surface Modification

Scanning electron microscopy was performed with a Hitachi SU8230 FE-SEM. Bare LSCF and PrO_x modified LSCF cells were prepared for cross sectional SEM by fracturing an electrolyte-supported cell. STEM was performed with a Hitachi HD-2700 operating at 200 kV. Scanning transmission electron microscope samples were prepared by scraping the cathode into a powder,

sonicating the powder in ethanol, and drying the solution on a TEM grid. The surface kinetic coefficient (k) was calculated using the electrical conductivity relaxation technique. QCM frequencies were measured with a Biolin Scientific QSense Analyzer. X-ray diffraction was performed with a Panalytical X'Pert PRO Alpha-1 diffractometer using Cu Kα1 radiation. To prepare the powders for XRD, 0.2 g of commercial LSCF was mixed with 0.37 g of $Pr(O^iPr)_3$ in 15 mL of anhydrous 2-ME, before adding 15 mL of DI water. The solution was died at 100 °C and fired at 650 °C for 10 hours. The experiment was repeated without LSCF, and fired at 500 °C and 800 °C.

Supporting Information

Electronic Supporting Information is available online.

Acknowledgements

N.K. and Y.Z. contributed equally to this work. M.L. conceived and supported the project. N.K. fabricated the symmetrical cells, performed the SSG coatings, characterized the cells and coatings, and wrote the draft. Y.Z. fabricated and measured the single cells. W.Z. performed the ECR measurement. Y.D. performed the TEM analysis. X.H. assisted with DRT analysis. M.L., N.K., W.Z., Y.Z., and Z.L. revised the manuscript.

This work was supported by the U.S. Department of Energy Solid Oxide Fuel Cell Program under the award number DE-FE0031201 and Office of Energy Efficiency and Renewable Energy (EERE) Hydrogen and Fuel Cell R&D Program under the award number DE-EE0008439.

Conflict of Interest

The authors declare no conflict of interest.

References

1. D. Ding, X. X. Li, S. Y. Lai, K. Gerdes and M. L. Liu, *Energy & Environmental Science*, 2014, **7**, 552-575.
2. D. Oh, D. Gostovic and E. D. Wachsman, *Journal of Materials Research*, 2012, **27**, 1992-1999.
3. Y. Liu, K. Chen, L. Zhao, B. Chi, J. Pu, S. P. Jiang and L. Jian, *International Journal of Hydrogen Energy*, 2014, **39**, 15868-15876.
4. K. Chen, N. Ai and S. P. Jiang, *ECS Transactions*, 2015, **68**, 995-1002.
5. K. Chen, N. Ai, K. M. O'Donnell and S. P. Jiang, *Phys Chem Chem Phys*, 2015, **17**, 4870-4874.
6. Y. Chen, Y. M. Choi, S. Yoo, Y. Ding, R. Q. Yan, K. Pei, C. Qu, L. Zhang, I. Chang, B. T. Zhao, Y. X. Zhang, H. J. Chen, Y. Chen, C. H. Yang, B. deGlee, R. Murphy, J. Liu and M. L. Liu, *Joule*, 2018, **2**, 938-949.
7. Y. Chen, S. Yoo, X. X. Li, D. Ding, K. Pei, D. C. Chen, Y. Ding, B. T. Zhao, R. Murphy, B. Deglee, J. Liu and M. L. Liu, *Nano Energy*, 2018, **47**, 474-480.
8. J. Irvine, J. L. M. Rupp, G. Liu, X. Xu, S. Haile, X. Qian, A. Snyder, R. Freer, D. Ekren, S. Skinner, O. Celikbilek, S. Chen, S. Tao, T. H. Shin, R. O'Hayre, J. Huang, C. Duan, M. Papac, S. Li, V. Celorrio, A. Russell, B. Hayden, H. Nolan, X. Huang, G. Wang, I. Metcalfe, D. Neagu and S. G. Martín, *Journal of Physics: Energy*, 2021, **3**, 031502.
9. M. Zhang, G. Jeerh, P. Zou, R. Lan, M. Wang, H. Wang and S. Tao, *Materials Today*, 2021, **49**, 351-377.
10. Y. Chen, S. Yoo, W. L. Zhang, J. H. Kim, Y. C. Zhou, K. Pei, N. Kane, B. T. Zhao, R. Murphy, Y. Choi and M. L. Liu, *Acs Catalysis*, 2019, **9**, 7137-7142.
11. M. Y. Lu, R. Scipioni, B. K. Park, T. R. Yang, Y. A. Chart and S. A. Barnett, *Materials Today Energy*, 2019, **14**, 100362.
12. K. Pei, Y. Zhou, K. Xu, Z. He, Y. Chen, W. Zhang, S. Yoo, B. Zhao, W. Yuan, M. Liu and Y. Chen, *Nano Energy*, 2020, **72**, 104704.
13. Y. Niu, Y. Zhou, W. Lv, Y. Chen, Y. Zhang, W. Zhang, Z. Luo, N. Kane, Y. Ding, L. Soule, Y. Liu, W. He and M. Liu, *Advanced Functional Materials*, 2021, **31**, 2100034.
14. Y. C. Zhou, W. L. Zhang, N. Kane, Z. Y. Luo, K. Pei, K. Sasaki, Y. M. Choi, Y. Chen, D. Ding and M. L. Liu, *Advanced Functional Materials*, 2021, **31**, 2105386.
15. W. Zhang, Y. Zhou, A. M. Hussain, D. Song, Y. Miura, Y. Chen, Z. Luo, N. Kane, Y. Niu, N. Dale, Y. Fukuyama and M. Liu, *ACS Appl Mater Interfaces*, 2021, **13**, 4993-4999.
16. I. Ichinose, H. Senzu and T. Kunitake, *Chem Lett*, 1996, **25**, 831-832.
17. I. Ichinose, H. Senzu and T. Kunitake, *Chem Mater*, 1997, **9**, 1296-1298.
18. I. J. Gomez, W. B. Goodwin, D. Sabo, Z. J. Zhang, K. H. Sandhage and J. C. Meredith, *Journal of Materials Chemistry C*, 2015, **3**, 632-643.
19. W. Brandon Goodwin, I. J. Gomez, Y. Fang, J. C. Meredith and K. H. Sandhage, *Chem Mater*, 2013, **25**, 4529-4536.
20. G. J. Wang, Y. N. Fang, P. Kim, A. Hayek, M. R. Weatherspoon, J. W. Perry, K. H. Sandhage, S. R. Marder and S. C. Jones, *Advanced Functional Materials*, 2009, **19**, 2768-2776.
21. M. R. Weatherspoon, Y. Cai, M. Crne, M. Srinivasarao and K. H. Sandhage, *Angew Chem Int Ed Engl*, 2008, **47**, 7921-7923.

22. A. Thompson, D. Attwood, E. Gullikson, M. Howells, J. Kortright, A. Robinson, J. Underwood, K.-J. Kim, J. Kirz, I. Lindau, Y. Liu, P. Pianetta, J. Scofield, G. Williams and H. Winick, X-Ray Data Booklet, https://xdb.lbl.gov/, (accessed 10/21/2021, 2021).
23. H. Wang, W. Zhang, K. Guan, Z. Wei, J. Meng, J. Meng and X. Liu, *ACS Sustainable Chemistry & Engineering*, 2020, **8**, 3367-3380.
24. J. Hoϕjberg and M. Soϕgaard, *Electrochemical and Solid-State Letters*, 2011, **14**, B77-B79.
25. F. Liang, J. Chen, S. P. Jiang, B. Chi, J. Pu and L. Jian, *Electrochemistry Communications*, 2009, **11**, 1048-1051.
26. D. Ding, M. Gong, C. Xu, N. Baxter, Y. Li, J. Zondlo, K. Gerdes and X. Liu, *Journal of Power Sources*, 2011, **196**, 2551-2557.
27. S. P. Jiang, Y. Ye, T. He and S. B. Ho, *Journal of Power Sources*, 2008, **185**, 179-182.
28. L. Nie, M. Liu, Y. Zhang and M. Liu, *Journal of Power Sources*, 2010, **195**, 4704-4708.
29. T. Klemensø, C. Chatzichristodoulou, J. Nielsen, F. Bozza, K. Thydén, R. Kiebach and S. Ramousse, *Solid State Ionics*, 2012, **224**, 21-31.
30. Y. Chen, Y. Chen, D. Ding, Y. Ding, Y. Choi, L. Zhang, S. Yoo, D. C. Chen, B. Deglee, H. Xu, Q. Y. Lu, B. T. Zhao, G. Vardar, J. Y. Wang, H. Bluhm, E. J. Crumlin, C. H. Yang, J. Liu, B. Yildiz and M. L. Liu, *Energy & Environmental Science*, 2017, **10**, 964-971.
31. Y. Chen, S. Yoo, Y. Choi, J. H. Kim, Y. Ding, K. Pei, R. Murphy, Y. X. Zhang, B. T. Zhao, W. L. Zhang, H. J. Chen, Y. Chen, W. Yuan, C. H. Yang and M. L. Liu, *Energy & Environmental Science*, 2018, **11**, 2458-2466.
32. M. Li, Z. Sun, W. Yang, T. Hong, Z. Zhu, Y. Zhang, X. Wu and C. Xia, *Phys Chem Chem Phys*, 2016, **19**, 503-509.
33. Y. X. Zhang, Y. Chen, M. F. Yan and F. L. Chen, *Journal of Power Sources*, 2015, **283**, 464-477.
34. X. Zhang, W. Wu, Z. Zhao, B. Tu, D. Ou, D. Cui and M. Cheng, *Catalysis Science & Technology*, 2016, **6**, 4945-4952.
35. S. Wang, B. Wei and Z. Lü, *International Journal of Hydrogen Energy*, 2021, **46**, 30101-30111.
36. M. J. Jørgensen and M. Mogensen, *Journal of The Electrochemical Society*, 2001, **148**, A433-A442.
37. D. Ding, M. F. Liu, Z. B. Liu, X. X. Li, K. Blinn, X. B. Zhu and M. L. Liu, *Advanced Energy Materials*, 2013, **3**, 1149-1154.
38. M. E. Lynch, L. Yang, W. Qin, J.-J. Choi, M. Liu, K. Blinn and M. Liu, *Energy & Environmental Science*, 2011, **4**, 2249-2258.
39. E. H. Kim, H. J. Jung, K. S. An, J. Y. Park, J. Lee, I. D. Hwang, J. Y. Kim, M. J. Lee, Y. Kwon and J. H. Hwang, *Ceramics International*, 2014, **40**, 7817-7822.
40. Y. Chen, A. Hinerman, L. Liang, K. Gerdes, S. P. Navia, J. Prucz and X. Y. Song, *Journal of Power Sources*, 2018, **405**, 45-50.
41. H. J. Choi, K. Bae, S. Grieshammer, G. D. Han, S. W. Park, J. W. Kim, D. Y. Jang, J. Koo, J. W. Son, M. Martin and J. H. Shim, *Advanced Energy Materials*, 2018, **8**, 1802506.
42. Y. Chen, S. A. Paredes-Navia, C. O. Romo-De-La-Cruz, L. Liang, A. Fernandes, A. Hinerman, J. Prucz, M. Williams and X. Y. Song, *Journal of Power Sources*, 2021, **499**.